ADVANCED FUNCTIONAL MATERIALS
www.afm-journal.de



# Enhanced Device Performance of Perovskite Photovoltaics by Magnetic Field-Aligned Perovskites-Magnetic Nanoparticles Composite Thin Film

*Wenzhan Xu, Tao Zhu, Yongrui Yang, Luyao Zheng, Lei Liu, and Xiong Gong**

**Perovskite photovoltaics have drawn great attention in both academic and industrial sectors in the past decade. To date, impressive device performance has been achieved in state-of-the-art device architectures through morphological manipulation and generic interface engineering. In this study, enhanced device performance of perovskite photovoltaics by magnetic field-aligned $CH_3NH_3PbI_3$-mixed $Fe_3O_4$ magnetic nanoparticles ($CH_3NH_3PbI_3$:$Fe_3O_4$) composite thin films is reported. It is found that magnetic field-aligned $CH_3NH_3PbI_3$:$Fe_3O_4$ composite thin films possess superior film morphology, boosted and balanced charge carrier mobility, and suppressed trap density. Moreover, perovskite photovoltaics by magnetic field-aligned $CH_3NH_3PbI_3$:$Fe_3O_4$ composite thin films exhibit suppressed charge carrier recombination and shorter charge carrier extraction time. As a result, perovskite solar cells by magnetic field-aligned $CH_3NH_3PbI_3$:$Fe_3O_4$ composite thin films exhibit 20.23% power conversion efficiency with significantly reduced photocurrent hysteresis. Moreover, perovskite photodetectors by magnetic field-aligned $CH_3NH_3PbI_3$:$Fe_3O_4$ composite thin films exhibit a photoresponsivity of 858 mA $W^{-1}$, a photodetectivity over $10^{13}$ Jones (1 Jones = 1 cm $Hz^{1/2}$ $W^{-1}$) and a linear dynamic range over 160 dB at room temperature. All these device performance parameters are significantly better than those by pristine $CH_3NH_3PbI_3$ thin film. Thus, these studies provide a facile way to boost device performance of perovskite photovoltaics.**

## 1. Introduction

Hybrid perovskites have recently emerged as promising photovoltaic materials for approaching efficient perovskite solar cells (PSCs)[1–4] and ultrasensitive perovskite photodetectors (PPDs)[5–7] due to the low exciton binding energy, long charge carrier diffusion length, and high charge carrier mobility of perovskite materials, and the possibility of cost-effective high-throughput manufacturing of perovskite photovoltaics.[8–16] An impressive device performance has been reported from the state-of-the-art device architectures through morphological manipulation and generic interface engineering.[17–24] Studies indicated that the defect-assisted charge carrier recombination in perovskite photoactive layer was one of issues needs to be resolved for further boosting device performance.[8–16] Utilization of Lewis acid and/or Lewis base to passivate the surface defect has been attempted to address above issues, and boosted device performance was indeed observed from perovskite photovoltaics.[25–27]

Magnetic nanoparticles (MNPs) and external magnetic field (EMF) have been applied for enhancing electroluminescence and photoluminescence efficiencies, and photocurrent in optoelectronics.[28–33] It was found that quantum efficiencies from polymer light-emitting devices can be dramatically enhanced as conjugated polymers were incorporated with CoFe MNPs.[29] Zhang et al. reported an enhanced short-circuit current ($J_{SC}$) from organic photovoltaics (OPVs) as conjugated polymers were incorporated with $Fe_3O_4$ MNPs and further proposed that such enhancement was attributed to increased population of the triplet excitons induced by the superparamagnetism of $Fe_3O_4$ MNPs.[30] We observed that over 40% enhanced power conversion efficiencies (PCEs) from OPVs by EMF-aligned bulk heterojunction (BHJ) composite were mixed with $Fe_3O_4$ MNPs thin films and found out that such enhancement was attributed to reduced charge carrier recombination and charge carrier transport resistance, enhanced charge carrier mobility, and superior film morphology of BHJ composites thin films.[31] Müller–Buschbaum revealed that enhanced PCEs from BHJ OPVs with the presence of $Fe_3O_4$ MNPs were attributed to reduced recombination current by increased spin–orbit coupling.[32] Numerous reports have indicated that an EMF plays a role in perovskite devices,[34–36] but perovskite photovoltaics by perovskites mixed with MNPs and further aligned by an EMF was rarely reported.

In this study, we report boosted device performance of perovskite photovoltaics (PSCs and PPDs) by the EMF-aligned $CH_3NH_3PbI_3$-mixed $Fe_3O_4$ MNPs ($CH_3NH_3PbI_3$:$Fe_3O_4$) composite thin films. We find that the EMF-aligned $CH_3NH_3PbI_3$:$Fe_3O_4$ composite thin films possess superior

Dr. W. Xu, T. Zhu, Y. Yang, L. Zheng, Dr. L. Liu, Prof. X. Gong
Department of Polymer Engineering
College of Polymer Science and Polymer Engineering
The University of Akron
Akron, OH 44325, USA
E-mail: xgong@uakron.edu

The ORCID identification number(s) for the author(s) of this article can be found under https://doi.org/10.1002/adfm.202002808.

DOI: 10.1002/adfm.202002808

 

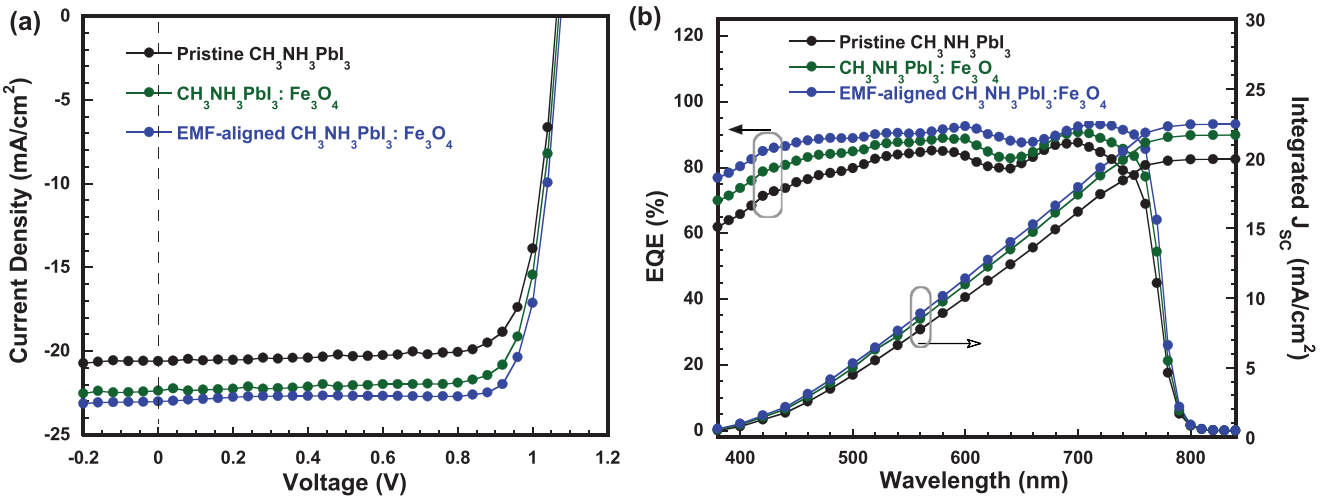


**Figure 1.** a) The *J–V* characteristics of PSCs under the reverse scan direction (from positive bias to negative bias), and b) the EQE spectra and the integrated current densities of PSCs by either pristine $CH_3NH_3PbI_3$ thin film, or the $CH_3NH_3PbI_3$:$Fe_3O_4$ thin film, or the EMF-aligned $CH_3NH_3PbI_3$:$Fe_3O_4$ thin film.

film morphology, boosted charge carrier mobility, and suppressed trap density. We also find that perovskite photovoltaics by the EMF-aligned $CH_3NH_3PbI_3$:$Fe_3O_4$ composite thin films exhibit suppressed charge carrier recombination and shorter charge carrier extraction time. As a result, PSCs by the EMF-aligned $CH_3NH_3PbI_3$:$Fe_3O_4$ composite thin films exhibit 20.23% PCEs with significantly reduced photocurrent hysteresis. Moreover, at room temperature, PPDs by the EMF-aligned $CH_3NH_3PbI_3$:$Fe_3O_4$ composite thin films exhibit a photoresponsivity of 858 mA W$^{-1}$, a photodetectivity over $10^{13}$ Jones (1 Jones = 1 cm Hz$^{1/2}$ W$^{-1}$), and a linear dynamic range over 160 dB.

## 2. Results and Discussions

**Figure 1**a presents the current density–voltage (*J–V*) characteristics of PSCs with a device configuration of ITO/PTAA/perovskite/$PC_{61}BM$/BCP/Al, where ITO is indium tin oxide and acts as the anode, PTAA is poly[bis(4-phenyl)(2,4,6-trimethylphenyl) amine] and acts as the hole extraction layer, $PC_{61}BM$ is phenyl-C61-butyric acid methyl ester and acts as the electron extraction layer, perovskite layer is either pristine $CH_3NH_3PbI_3$ thin film, or the $CH_3NH_3PbI_3$:$Fe_3O_4$ MNPs thin film ($CH_3NH_3PbI_3$:$Fe_3O_4$ composite thin film), or the EMF-aligned $CH_3NH_3PbI_3$:$Fe_3O_4$ MNPs thin film (EMF-aligned $CH_3NH_3PbI_3$:$Fe_3O_4$ composite thin film), BCP is bathocuproine and is used as the hole blocking layer, Al is aluminum and acts as the cathode, respectively. The synthetic procedure of $Fe_3O_4$ MNPs was reported in previous publication.[37] The characterization of $Fe_3O_4$ MNPs is described in Section S1 in the Supporting Information. The fabrication processes of PSCs by the EMF-aligned $CH_3NH_3PbI_3$:$Fe_3O_4$ composite thin film are described in the Experimental Section and Section S2 in the Supporting Information. The effects of $Fe_3O_4$ MNP sizes, the EMF intensities, and the concentrations of $Fe_3O_4$ MNPs on device performance of PSCs by the EMF-aligned $CH_3NH_3PbI_3$:$Fe_3O_4$ composite thin films are described in Section S3 in the Supporting Information. The device performance parameters of PSCs under white light illumination with the light intensity of 100 mW cm$^{-2}$ and under the reverse scan direction at a scan rate of 0.60 V s$^{-1}$ are summarized in **Table 1**. The PSCs by pristine $CH_3NH_3PbI_3$ thin film exhibit an open-circuit voltage ($V_{OC}$) of 1.08 V, a $J_{SC}$ of 20.61 mA cm$^{-2}$, a fill factor (FF) of 79.5%, and a corresponding PCE of 17.69%. These device performance parameters are in good agreement with those from PSCs with similar device structures.[38–42] The PSCs by the EMF-aligned $CH_3NH_3PbI_3$ thin film exhibit a $V_{OC}$ of 1.08 V, a $J_{SC}$ of 20.68 mA cm$^{-2}$, an FF of 79.8%, and a corresponding PCE of 17.82%, which is almost the same as that by pristine $CH_3NH_3PbI_3$ thin film. The PSCs by the $CH_3NH_3PbI_3$:$Fe_3O_4$ composite thin film exhibit a $V_{OC}$ of 1.08 V, a $J_{SC}$ of 22.38 mA cm$^{-2}$, an FF of 80.3%, and a corresponding PCE of 19.41%. Whereas PSCs by the EMF-aligned $CH_3NH_3PbI_3$:$Fe_3O_4$ composite thin film exhibit a $V_{OC}$ of 1.08 V, a $J_{SC}$ of 23.02 mA cm$^{-2}$, an FF of 81.4%, and a corresponding PCE of 20.23%, which is ≈15% enhancement as compared with

**Table 1.** Device performance parameters of PSCs.

| Photoactive layers | $V_{OC}$ [V] | $J_{SC}$ [mA cm$^{-2}$] | FF [%] | PCE[a)] [%] | PCE[b)] [%] | $R_S$ [Ω cm$^2$] | $R_{SH}$ [Ω cm$^2$] |
|---|---|---|---|---|---|---|---|
| Pristine $CH_3NH_3PbI_3$ | 1.08 | 20.61 | 79.5 | 17.69 | 17.28 | 14 | 898 |
| $CH_3NH_3PbI_3$:$Fe_3O_4$ | 1.08 | 22.38 | 80.3 | 19.41 | 19.25 | 9 | 1067 |
| EMF-aligned $CH_3NH_3PbI_3$:$Fe_3O_4$ | 1.08 | 23.02 | 81.4 | 20.23 | 19.96 | 7 | 1283 |

[a)]The best PCEs; [b)]The average PCEs from over 50 identical pixels, respectively.

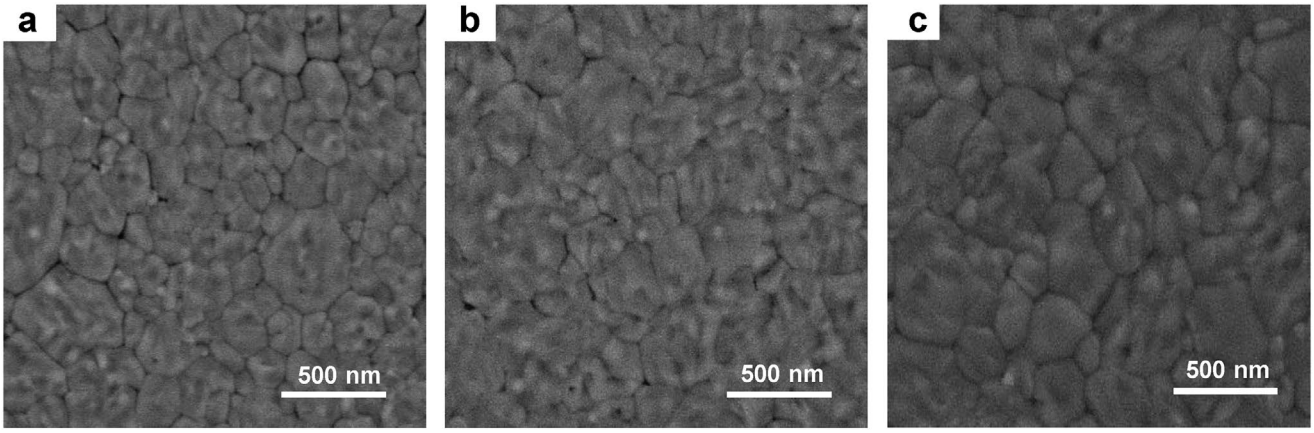


**Scheme 1.** The SEM images of a) pristine $CH_3NH_3PbI_3$ thin film, b) the $CH_3NH_3PbI_3$:$Fe_3O_4$ thin film, and c) the EMF-aligned $CH_3NH_3PbI_3$:$Fe_3O_4$ thin film.

that by pristine $CH_3NH_3PbI_3$ thin film. It is found that major boosted device performance parameters are $J_{SC}$ and FF. Noted that ten devices, each device has five identical pixels, are fabricated and characterized. The average PCEs observed from 50 identical pixels are summarized in Table 1.

The external quantum efficiency (EQE) spectra of PSCs are shown in Figure 1b. As compared with PSCs by pristine $CH_3NH_3PbI_3$ thin film, the EQE spectra of PSCs by the $CH_3NH_3PbI_3$:$Fe_3O_4$ composite thin film and PSCs by the EMF-aligned $CH_3NH_3PbI_3$:$Fe_3O_4$ composite thin film reveal enhancement in the wavelength ($\lambda$) ranging from 380 to 780 nm. The integrated $J_{SC}$ values from the EQE spectra are 19.95, 21.69, and 22.47 mA $cm^{-2}$ for PSCs by pristine $CH_3NH_3PbI_3$, PSCs by the $CH_3NH_3PbI_3$:$Fe_3O_4$ composite thin film, and PSCs by the EMF-aligned $CH_3NH_3PbI_3$:$Fe_3O_4$ composite thin film, respectively. Theses $J_{SC}$ values are in good agreement with those extracted from the $J$–$V$ characteristics (Figure 1a).

To understand underlying physics of enhanced $J_{SC}$ from PSCs by the $CH_3NH_3PbI_3$:$Fe_3O_4$ composite thin film and PSCs by the EMF-aligned $CH_3NH_3PbI_3$:$Fe_3O_4$ composite thin film, the absorption spectra of different perovskite thin films are first conducted (Section S4, Supporting Information). Negligible change observed from the absorption spectra indicates that neither $Fe_3O_4$ MNPs nor further an EMF alignment has effects on the absorption profiles of $CH_3NH_3PbI_3$ thin films.

**Scheme 1** displays scanning electron microscope (SEM) images of pristine $CH_3NH_3PbI_3$ thin film, the $CH_3NH_3PbI_3$:$Fe_3O_4$ composite thin film, and the EMF-aligned $CH_3NH_3PbI_3$:$Fe_3O_4$ composite thin film. Pristine $CH_3NH_3PbI_3$ thin film exhibits large pinholes and voids. The crystal domains of $CH_3NH_3PbI_3$ thin film are prone to be aggregated, rendering a rough surface morphology. Such rough surface could act as the leakage current pathways, resulting in low photocurrent.[43–46] The $CH_3NH_3PbI_3$:$Fe_3O_4$ composite thin film exhibits uniform crystal domains with less uncovered areas. Moreover, the EMF-aligned $CH_3NH_3PbI_3$:$Fe_3O_4$ composite thin film possesses dramatically reduced uncovered areas than that of the $CH_3NH_3PbI_3$:$Fe_3O_4$ composite thin film. Both pinhole size and pinhole proportion in perovskite thin films are further analyzed statistically based on the SEM images (Section S5, Supporting Information). Pristine $CH_3NH_3PbI_3$ thin film possesses large numbers of large-size pinholes, whereas, the $CH_3NH_3PbI_3$:$Fe_3O_4$ composite thin film has decreased numbers of large-size pinholes and reduced overall pinhole area. Moreover, the EMF-aligned $CH_3NH_3PbI_3$:$Fe_3O_4$ composite thin film exhibits limited small-size pinholes with 98% surface coverage. The pinholes and surface defects in perovskite thin films could induce severe charge carrier recombination, resulting in decreased $J_{SC}$ and FF.[47–49] Superior film morphology observed from both the $CH_3NH_3PbI_3$:$Fe_3O_4$ composite thin film and the EMF-aligned $CH_3NH_3PbI_3$:$Fe_3O_4$ composite thin film indicates that PSCs by either the $CH_3NH_3PbI_3$:$Fe_3O_4$ composite thin film or the EMF-aligned $CH_3NH_3PbI_3$:$Fe_3O_4$ composite thin film exhibit enhanced $J_{SC}$ and FF, thus high PCEs.[50]

The grazing-incidence wide-angle X-ray scattering (GIWAXS) study is carried out to get insight into film morphology and the crystallographic orientations of perovskite thin films. **Figure 2**a–d shows the 2D GIWAXS patterns of pristine $CH_3NH_3PbI_3$ thin film, the EMF-aligned $CH_3NH_3PbI_3$ thin film, the $CH_3NH_3PbI_3$:$Fe_3O_4$ composite thin film, and the EMF-aligned $CH_3NH_3PbI_3$:$Fe_3O_4$ composite thin film. It is found that both pristine $CH_3NH_3PbI_3$ thin film and the EMF-aligned $CH_3NH_3PbI_3$ thin film possess nearly the same GIWAXS patterns. Strong scattering rings, corresponding to the polycrystalline structures, are presented in $CH_3NH_3PbI_3$ and the EMF-aligned $CH_3NH_3PbI_3$ thin films. These results indicate that the EMF alignment has no effect on the crystallinity of $CH_3NH_3PbI_3$ thin film. Whereas, the emerged rings due to the existence of $Fe_3O_4$ MNPs and highly oriented crystal domains from $CH_3NH_3PbI_3$ thin film are observed along the in-plane direction (Figure 2c) from the $CH_3NH_3PbI_3$:$Fe_3O_4$ composite thin film and the EMF-aligned $CH_3NH_3PbI_3$:$Fe_3O_4$ composite thin film, indicating that a highly aligned perovskite crystal pattern is formed in the $CH_3NH_3PbI_3$:$Fe_3O_4$ composite thin film and the EMF-aligned $CH_3NH_3PbI_3$:$Fe_3O_4$ composite thin film. Remarkably, even much stronger oriented perovskite crystal domains along the in-plane direction (Figure 2d) are observed from the EMF-aligned $CH_3NH_3PbI_3$:$Fe_3O_4$ composite thin film, which reveals that more oriented and less amorphous perovskite crystal structure are formed in the EMF-aligned $CH_3NH_3PbI_3$:$Fe_3O_4$ composite thin film. All these results demonstrate that $Fe_3O_4$ MNPs with an EMF alignment could facilitate the perovskite crystallization process, resulting in highly ordered perovskite crystal structure. As a result, PSCs by the

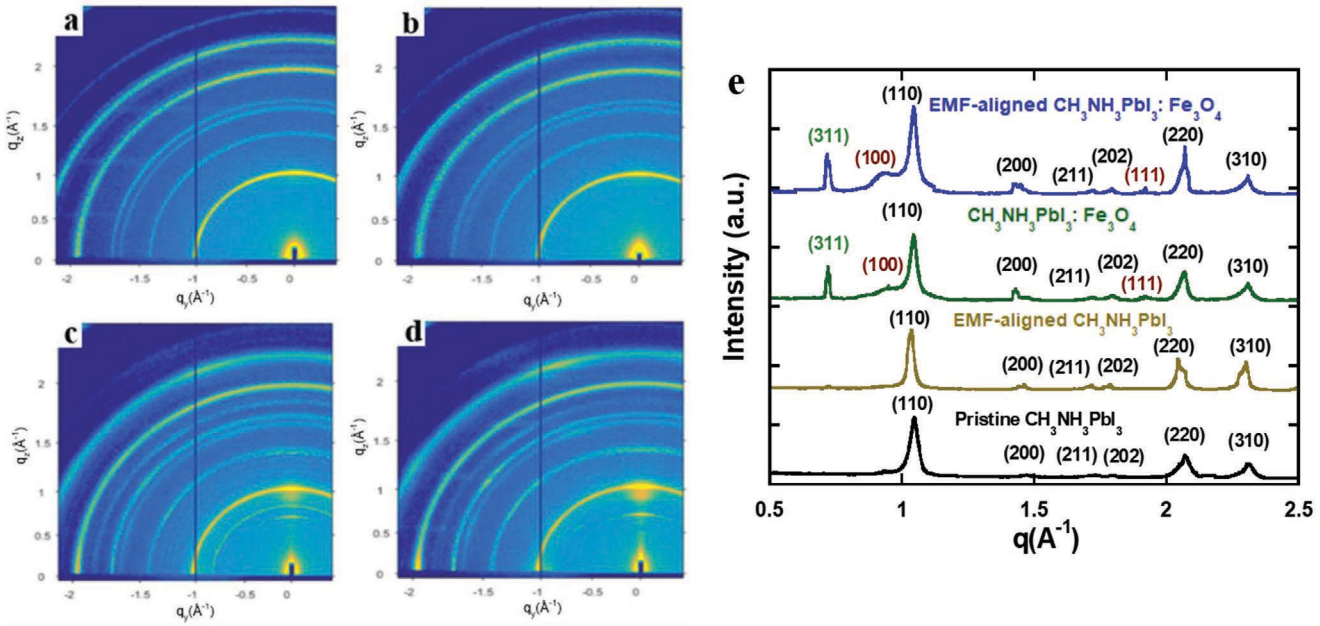


**Figure 2.** The 2D GIWAXS patterns of a) pristine $CH_3NH_3PbI_3$ thin film, b) the EMF-aligned $CH_3NH_3PbI_3$ thin film, c) the $CH_3NH_3PbI_3$:$Fe_3O_4$ thin film, and d) the EMF-aligned $CH_3NH_3PbI_3$:$Fe_3O_4$ thin film, e) the azimuthal integral of 2D GIWAXS pattern of pristine $CH_3NH_3PbI_3$ thin film, the EMF-aligned $CH_3NH_3PbI_3$ thin film, the $CH_3NH_3PbI_3$:$Fe_3O_4$ thin film, and the EMF-aligned $CH_3NH_3PbI_3$:$Fe_3O_4$ thin film.

$CH_3NH_3PbI_3$:$Fe_3O_4$ composite thin film exhibit increased $J_{SC}$ and enlarged FF, consequently enhanced PCE, and PSCs by the EMF-aligned $CH_3NH_3PbI_3$:$Fe_3O_4$ composite thin film exhibit even more increased $J_{SC}$ and enlarged FF, consequently dramatically enhanced PCEs.

Figure 2e presents the azimuthal integral of 2D GIWAXS patterns of pristine $CH_3NH_3PbI_3$ thin film, the EMF-aligned $CH_3NH_3PbI_3$ thin film, the $CH_3NH_3PbI_3$:$Fe_3O_4$ composite thin film, and the EMF-aligned $CH_3NH_3PbI_3$:$Fe_3O_4$ composite thin film. Three major peaks, corresponding to the (110), (220), and (310) lattice planes, are observed from all these four different $CH_3NH_3PbI_3$ thin films, which indicate that $CH_3NH_3PbI_3$ thin films possess the tetragonal crystal structure.[51,52] But the intensities of above three lattice plans for the EMF-aligned $CH_3NH_3PbI_3$:$Fe_3O_4$ composite thin film are slightly higher than those for pristine $CH_3NH_3PbI_3$ thin film, which implies that the EMF-aligned $CH_3NH_3PbI_3$:$Fe_3O_4$ composite thin film possesses more slightly better crystallinity than those of pristine $CH_3NH_3PbI_3$ thin film. Moreover, a new peak located at $q$ = 0.75 $Å^{-1}$, corresponding to the existence of $Fe_3O_4$ MNPs, is observed from the $CH_3NH_3PbI_3$:$Fe_3O_4$ composite thin film and the EMF-aligned $CH_3NH_3PbI_3$:$Fe_3O_4$ composite thin film, indicating that $Fe_3O_4$ MNPs are physically mixed within $CH_3NH_3PbI_3$ thin film. In addition, two new peaks located at $q$ = 0.9 and 1.9 $Å^{-1}$, corresponding to the (100) plane and the (111) plane, respectively, are observed from the $CH_3NH_3PbI_3$:$Fe_3O_4$ composite thin film and the EMF-aligned $CH_3NH_3PbI_3$:$Fe_3O_4$ composite thin film. These results indicate that the $CH_3NH_3PbI_3$:$Fe_3O_4$ thin film and the EMF-aligned $CH_3NH_3PbI_3$:$Fe_3O_4$ composite thin film possess both the tetragonal crystal structure and the cubic crystal structure.[41] In addition, it is found that with an EMF alignment, the intensities of the (100) and (111) planes are enhanced, implies that the cubic crystal structure is more ordered in the EMF-aligned $CH_3NH_3PbI_3$:$Fe_3O_4$ composite thin films. It was reported that perovskite with the cubic crystal structure possesses enhanced electrical conductivity compared to that with the tetragonal crystal structure,[41] which would result in enhanced $J_{SC}$ and enlarged FF. As a result, enhanced PCE is observed from PSCs by the $CH_3NH_3PbI_3$:$Fe_3O_4$ composite thin film and significantly enhanced PCE is observed from PSCs by the EMF-aligned $CH_3NH_3PbI_3$:$Fe_3O_4$ composite thin film.

The charge carrier transport properties in $CH_3NH_3PbI_3$ thin films are evaluated by charge carrier trap density and charge carrier mobility based on the trap-filling limited (TFL) and the space-charge limited current (SCLC) methods, respectively, according to the Mott–Gurney law.[53,54] The hole-only device with a structure of ITO/PTAA/perovskite/$MoO_3$/Ag and the electron-only device with a structure of ITO/Al/perovskite/Al, where $MoO_3$ is molybdenum trioxide and used as the electron blocking layer, and Ag is sliver and used as the electrode, respectively, are fabricated and characterized. As presented in Section S6 in the Supporting Information, an Ohmic contact regime is depicted by the linear dark current densities versus the applied voltage ($J_d$–$V$) characteristics under low external voltage (where $J_d$ is the current density measured in dark); with dramatically increased current injection at middle applied voltage, a TFL regime is formed.[54,55] In TFL region, all the traps being filled up; followed with the TFL regime is the trap-free SCLC regime, which is also called Child's regime.[54] In the TFL regime, the charge carrier density of perovskite thin films can be estimated by $n_t = \frac{2\varepsilon\varepsilon_0 V_{TFL}}{eL^2}$,[56,57] where $n_t$ is the trap density, $\varepsilon$ (32) is relative dielectric constant of perovskite,[56] $\varepsilon_0$ is the vacuum permittivity, $e$ is the elementary charge, $L$ is the thickness of perovskite film, and $V_{TFL}$ is the onset voltage of the TFL, respectively. The

hole and electron trap densities are calculated and summarized in Section S6 in the Supporting Information. The hole trap density of the EMF-aligned $CH_3NH_3PbI_3$:$Fe_3O_4$ composite thin film is $8.2 \times 10^{15}$ $cm^{-3}$, which is nearly four times smaller than that ($3.1 \times 10^{16}$ $cm^{-3}$) for the $CH_3NH_3PbI_3$:$Fe_3O_4$ composite thin film and is approximatively ten times smaller than that ($7.5 \times 10^{16}$ $cm^{-3}$) of pristine $CH_3NH_3PbI_3$ thin film. The latter one is in good agreement with reported value.[58] The electron trap densities of $2.4 \times 10^{16}$, $1.1 \times 10^{16}$, and $3.3 \times 10^{15}$ $cm^{-3}$ are calculated for pristine $CH_3NH_3PbI_3$ thin film, the $CH_3NH_3PbI_3$:$Fe_3O_4$ composite thin film, and the EMF-aligned $CH_3NH_3PbI_3$:$Fe_3O_4$ composite thin film, respectively. The decreased trap densities for both the $CH_3NH_3PbI_3$:$Fe_3O_4$ composite thin film and the EMF-aligned $CH_3NH_3PbI_3$:$Fe_3O_4$ composite thin film indicate high quality of thin films and superior film morphology, which are favorable for charge carrier to be transported, resulting in suppressed charge carrier recombination. Thus, enlarged FF and $J_{SC}$ are observed from PSCs by either the $CH_3NH_3PbI_3$:$Fe_3O_4$ composite thin film or the EMF-aligned $CH_3NH_3PbI_3$:$Fe_3O_4$ composite thin film.

The charge carrier mobility ($\mu$) is estimated by $J_d = \frac{9\varepsilon\varepsilon_0\mu V_b^2}{8L^3}$,[59] where $J_d$ is the dark current density and $V_b$ is the built-in potential. The charge carrier mobilities are summarized in Section S6 in the Supporting Information. The hole mobility for pristine $CH_3NH_3PbI_3$ thin film is $1.4 \times 10^{-3}$ $cm^2$ $V^{-1}$ $s^{-1}$, which is consistent with the reported value.[60] The hole mobilities for the $CH_3NH_3PbI_3$:$Fe_3O_4$ composite thin film and the EMF-aligned $CH_3NH_3PbI_3$:$Fe_3O_4$ composite thin film are $3.6 \times 10^{-3}$ and $1.34 \times 10^{-2}$ $cm^2$ $V^{-1}$ $s^{-1}$, respectively. The hole mobility for the EMF-aligned $CH_3NH_3PbI_3$:$Fe_3O_4$ composite thin film is approximatively four times larger than that for the $CH_3NH_3PbI_3$:$Fe_3O_4$ composite thin film, and approximatively one order magnitude larger than that for pristine $CH_3NH_3PbI_3$ thin film. The electron mobilities of $8.5 \times 10^{-3}$, $1.87 \times 10^{-2}$, and $3.30 \times 10^{-2}$ $cm^2$ $V^{-1}$ $s^{-1}$ are for pristine $CH_3NH_3PbI_3$ thin film, the $CH_3NH_3PbI_3$:$Fe_3O_4$ composite thin film, and the EMF-aligned $CH_3NH_3PbI_3$:$Fe_3O_4$ composite thin film, respectively. The electron mobility for the EMF-aligned $CH_3NH_3PbI_3$:$Fe_3O_4$ composite thin film is approximatively two times larger than that for the $CH_3NH_3PbI_3$:$Fe_3O_4$ composite thin film, and approximatively four times larger than that for pristine $CH_3NH_3PbI_3$ thin film. It is clear that both hole and electron mobilities of $CH_3NH_3PbI_3$ are simultaneously enhanced and balanced by $Fe_3O_4$ MNPs and further by an EMF alignment. Thus, as expected, enhanced $J_{SC}$ and enlarged FF, consequently boosted PCEs are observed from PSCs by the $CH_3NH_3PbI_3$:$Fe_3O_4$ composite thin film and PSCs by the EMF-aligned $CH_3NH_3PbI_3$:$Fe_3O_4$ composite thin film.

**Figure 3**a presents the time-resolved photoluminescence (TRPL) spectra of different $CH_3NH_3PbI_3$ thin films. The lifetimes ($t$) of charge carrier transporting for pristine $CH_3NH_3PbI_3$ thin film, the $CH_3NH_3PbI_3$:$Fe_3O_4$ composite thin film, and the EMF-aligned $CH_3NH_3PbI_3$:$Fe_3O_4$ composite thin film are estimated to be ≈94, ≈118, and ≈158 ns, respectively. According to the equation of $L_D = (kT\mu t/e)^{1/2}$ (where $L_D$ is the charge carrier diffusion length, $k$ is the Boltzmann constant, $T$ is the absolute temperature, $\mu$ is the carrier mobility of thin film, and $e$ is the elementary charge, respectively),[60] the $L_D$ for the EMF-aligned $CH_3NH_3PbI_3$:$Fe_3O_4$ composite thin film is the largest among these three ones due to higher charge carrier mobility and longer lifetime of charge carrier transporting. The long charge carrier diffusion length would ensure charge carriers to be efficiently transported from $CH_3NH_3PbI_3$ thin film to the electrodes, resulting in high $J_{SC}$ for PSCs.[60] Thus, PSCs by the EMF-aligned $CH_3NH_3PbI_3$:$Fe_3O_4$ composite thin film exhibit enhanced $J_{SC}$, thus boosted PCE.

The impedance spectroscopy (IS) is further carried out to investigate the internal series resistances ($R_S$) of PSCs, which is enabled to monitor the detailed electrical properties of the interfaces that cannot be determined by direct current measurements. The IS is conducted in dark and under an applied voltage close to $V_{OC}$ of PSCs. The $R_S$ consists of the sheet resistance ($R_{Sheet}$) of the electrodes, and the charge-transfer resistance ($R_{CT}$) at the interfaces between the electrode and the charge carrier extraction layers, as well as the interface between the charge carrier extraction layer and perovskite layer.[61–64] In this study, all PSCs have the same device structure; the only difference is in perovskite layer. Thus, the equivalent electric circuit (also called RC circuit model) shown in the inset of Figure 3b can be used to describe PSCs.[65] The Nyquist plots of PSCs measured in dark and under an applied voltage close to $V_{OC}$ of PSCs are displayed in Figure 3b. The semicircle confirms the accuracy of the RC circuit model and further indicates that each layer is relatively homogenous along with the transport pathways without discernible multiple interfacial boundaries.[65] Thus, the $R_{CT}$ values of PSCs by pristine $CH_3NH_3PbI_3$ thin film, PSCs by the $CH_3NH_3PbI_3$:$Fe_3O_4$ composite thin film, and PSCs by the EMF-aligned $CH_3NH_3PbI_3$:$Fe_3O_4$ composite thin film are ≈933, ≈748, and ≈560 Ω, respectively. The smaller $R_{CT}$ observed from PSCs by the EMF-aligned $CH_3NH_3PbI_3$:$Fe_3O_4$ composite thin film is originated from superior film morphology and smother surface of $CH_3NH_3PbI_3$ thin film induced by $Fe_3O_4$ MNPs and further aligned by an EMF. These results indicate that PSCs by the EMF-aligned $CH_3NH_3PbI_3$:$Fe_3O_4$ composite thin film exhibit high $J_{SC,}$ FF, and thus high PCE.

Figure 3c,d displays the steady-state light intensity-dependent $V_{OC}$ and $J_{SC}$ of PSCs. The relations between $V_{OC}$ and the light intensity is depicted as $V_{OC} \propto S\ln(I)$, where S is the slope and $I$ is the light intensity.[66,67] The $S$ values of PSCs by pristine $CH_3NH_3PbI_3$ thin film, PSCs by the $CH_3NH_3PbI_3$:$Fe_3O_4$ composite thin film, and PSCs by the EMF-aligned $CH_3NH_3PbI_3$:$Fe_3O_4$ composite thin film are 0.032, 0.030, and 0.027, respectively. The latter one is very close to $S = kT/q = 0.026$ (where $k$ is the Boltzmann's constant, $T$ is the temperature, and $q$ is the elementary charge at room temperature), which is an indication that the geminate recombination is significantly suppressed in PSCs by the EMF-aligned $CH_3NH_3PbI_3$:$Fe_3O_4$ composite thin film. In Figure 3d, a near-linear dependence of $J_{SC}$ with the light intensity for PSCs by the EMF-aligned $CH_3NH_3PbI_3$:$Fe_3O_4$ composite thin film is observed, with a coefficient of $\alpha = 0.98$ corresponding to the power law of $J_{SC} \propto I^{\alpha}$,[67] in contrast, both two other PSCs show a slightly nonlinear characteristics of $J_{SC}$ versus $I$ with the coefficient of $\alpha = 0.94$ and $\alpha = 0.92$, respectively. Different $\alpha$ values indicate that nongeminate recombination processes are different in these three PSCs. A nearly linear dependence of $J_{SC}$ with the light intensity implies that nongeminate recombination process is suppressed.[67] Therefore, PSCs by the

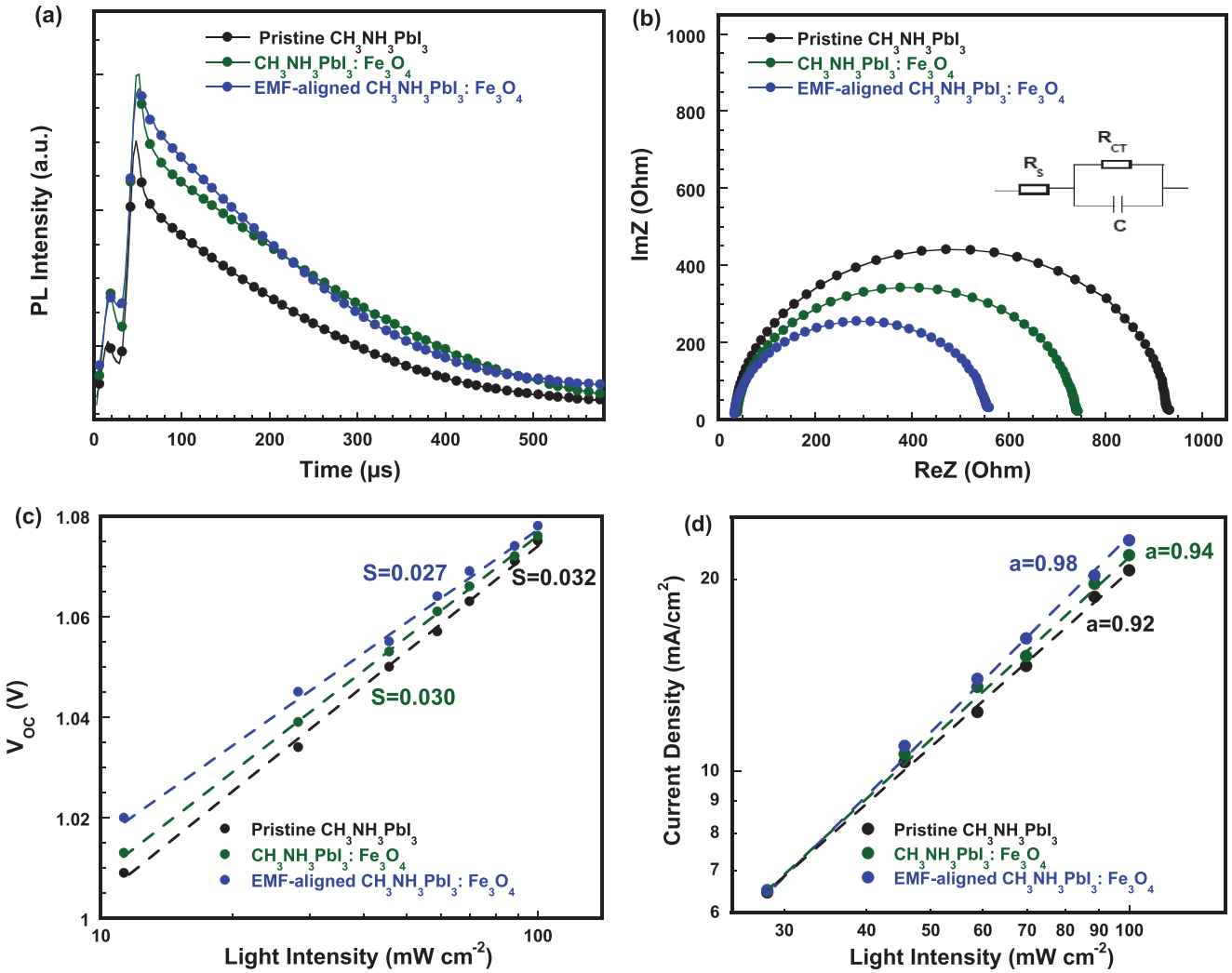


**Figure 3.** a) The TRPL spectra of PSCs, b) the Nyquist plots of PSCs measured in dark and under an applied voltage close to the open-circuit voltage of PSCs, and the light intensity dependent of c) the steady-state open circuit voltage (the dotted lines represent fits to the expression $V_{OC} = S\ln(I/I_0)$), and d) the steady-state short-circuit current (the dotted lines represent fits to the expression $J_{SC} \propto I^{\alpha}$) of PSCs, where PSCs are fabricated by either pristine $CH_3NH_3PbI_3$ thin film, or the $CH_3NH_3PbI_3$:$Fe_3O_4$ thin film, or the EMF-aligned $CH_3NH_3PbI_3$:$Fe_3O_4$ thin film.

EMF-aligned $CH_3NH_3PbI_3$:$Fe_3O_4$ composite thin film exhibit enlarged $J_{SC}$ and FF, and thus high PCE.

The transient photocurrent (TPC) measurement, a time-resolved technique, is performed to evaluate charge carrier collection efficiency in PSCs.[39–41,68,69] It is found that significantly increased photocurrent densities are observed from PSCs by the EMF-aligned $CH_3NH_3PbI_3$:$Fe_3O_4$ composite thin film (Section S7, Supporting Information). Such boosted photocurrent densities are ascribed to the suppressed charge carrier recombination. **Figure 4**a presents the normalized TPC curves of PSCs under an applied bias of −2 V. Under such high bias voltage, all charge carriers are swept out prior recombination. Charge carrier transit time is estimated by extrapolating the linear region to zero photocurrent.[65] It is found that the charge carrier extraction times from PSCs by pristine $CH_3NH_3PbI_3$ thin film, PSCs by the $CH_3NH_3PbI_3$:$Fe_3O_4$ composite thin film, and PSCs by the EMF-aligned $CH_3NH_3PbI_3$:$Fe_3O_4$ composite thin film are ≈164, ≈128, and ≈116 ns, respectively. The shorter charge carrier extraction time indicates that efficient charge carrier extraction process takes place in PSCs. Thus, PSCs by the EMF-aligned $CH_3NH_3PbI_3$:$Fe_3O_4$ composite thin film exhibit enhanced $J_{SC}$. Moreover, by the integration of the TPC densities over the transient times, the extracted charge carrier densities of PSCs versus the transient times are estimated and the results are shown in Figure 4b. It is found that the extracted charge carrier densities observed from PSCs by the EMF-aligned $CH_3NH_3PbI_3$:$Fe_3O_4$ composite thin film is higher than that by the $CH_3NH_3PbI_3$:$Fe_3O_4$ composite thin film, the latter one is higher than that by pristine $CH_3NH_3PbI_3$ thin film. As compared with the extracted charge carrier densities from PSCs by pristine $CH_3NH_3PbI_3$ thin film, ≈15% increased total extracted charge carrier densities were observed from PSCs by the EMF-aligned $CH_3NH_3PbI_3$:$Fe_3O_4$ composite thin film. Such observation is consistent with the results from the steady-state device efficiency, the *J*–*V* characteristics (Figure 1). Thus, PSCs by the EMF-aligned $CH_3NH_3PbI_3$:$Fe_3O_4$ composite thin film exhibit boosted PCE.

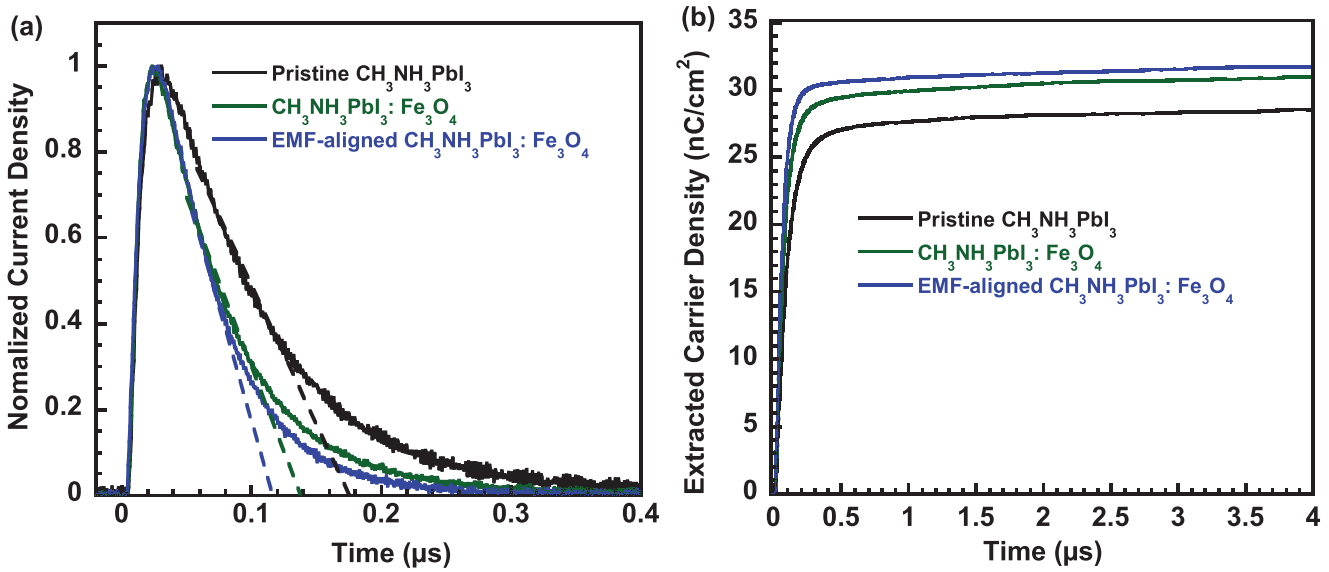


**Figure 4.** a) The normalized TPC curves and b) the integrated charge densities of PSCs by either pristine $CH_3NH_3PbI_3$ thin film, or the $CH_3NH_3PbI_3$:$Fe_3O_4$ thin film, or the EMF-aligned $CH_3NH_3PbI_3$:$Fe_3O_4$ thin film.

The effect of different scan rates on PCEs of PSCs is shown in **Figure 5**a. It is found that PCEs of all PSCs increase and then decrease along with the increased scan rates. This observation is in good agreement with other reports,[70,71] indicating that PSCs possess the photocurrent hysteresis behaviors. The photocurrent hysteresis behaviors are further investigated through the *J*–*V* characteristics of PSCs measured under different scan directions at a scan rate of 0.60 V $s^{-1}$ and the results are shown in Figure 5b–d. The photocurrent hysteresis is quantitatively described by the hysteresis index (HI), which is defined as $HI = \frac{PCE_{reverse} - PCE_{forward}}{PCE_{reverse}}$,[72] where $PCE_{reverse}$ and $PCE_{forward}$ are PCE of PSCs measured under the reserve and the forward directions. The HI values of 0.062, 0.031, and 0.018 are observed for PSCs by pristine $CH_3NH_3PbI_3$ thin film, PSCs by the $CH_3NH_3PbI_3$:$Fe_3O_4$ composite thin film, and PSCs by the EMF-aligned $CH_3NH_3PbI_3$:$Fe_3O_4$ composite thin film, respectively. It is obvious that PSCs by the EMF-aligned $CH_3NH_3PbI_3$:$Fe_3O_4$ composite thin film exhibit the smallest HI value. Such suppressed photocurrent hysteresis is probably ascribed to reduced trap states and tuned crystal structure, superior film morphology of the $CH_3NH_3PbI_3$:$Fe_3O_4$ composite thin film induced by $Fe_3O_4$ MNPs and an EMF alignment.[28–35]

The PPDs with the same device structure as that for PSCs is also investigated. **Figure 6**a presents the *J*–*V* characteristics of PPDs measured both in dark and under the monochromatic light at the wavelength of 500 nm with the light intensity of 0.28 mW $cm^{-2}$ at room temperature. The device performance parameters are summarized in **Table 2**. It is found that the photocurrent densities ($J_{ph}$) of PPDs by the EMF-aligned $CH_3NH_3PbI_3$:$Fe_3O_4$ composite thin film in the reverse bias region are higher than those by the $CH_3NH_3PbI_3$:$Fe_3O_4$ composite thin film. The latter are higher than those by pristine $CH_3NH_3PbI_3$ thin film. For example, $J_{ph}$ of $4.06 \times 10^{-5}$, $1.09 \times 10^{-4}$, and $2.40 \times 10^{-4}$ mA $cm^{-2}$ are observed from PPDs by pristine $CH_3NH_3PbI_3$ thin film, PPDs by the $CH_3NH_3PbI_3$:$Fe_3O_4$ composite thin film, and PPDs by the EMF-aligned $CH_3NH_3PbI_3$:$Fe_3O_4$ composite thin film, respectively. Such boosted $J_{ph}$ values are originated from enhanced charge transport properties of the EMF-aligned $CH_3NH_3PbI_3$:$Fe_3O_4$ composite thin film and the $CH_3NH_3PbI_3$:$Fe_3O_4$ composite thin film. Moreover, $J_d$ observed from PPDs by the EMF-aligned $CH_3NH_3PbI_3$:$Fe_3O_4$ composite thin film in the reverse bias region are lower than those by the $CH_3NH_3PbI_3$:$Fe_3O_4$ composite thin film. The latter are lower than those by pristine $CH_3NH_3PbI_3$ thin film. For example, under a bias of – 0.5 V, $J_d$ of $6.09 \times 10^{-9}$, $4.71 \times 10^{-9}$, and $3.84 \times 10^{-9}$ mA $cm^{-2}$ are observed from PPDs by pristine $CH_3NH_3PbI_3$ thin film, PPDs by the $CH_3NH_3PbI_3$:$Fe_3O_4$ composite thin film, and PPDs by the EMF-aligned $CH_3NH_3PbI_3$:$Fe_3O_4$ composite thin film, respectively. Such high $J_{ph}$ and low $J_d$ observed from PPDs by the EMF-aligned $CH_3NH_3PbI_3$:$Fe_3O_4$ composite thin film indicate that PPDs by the EMF-aligned $CH_3NH_3PbI_3$:$Fe_3O_4$ composite thin film possess high photosensitivity.[73]

The photoresponsivity (*R*) and projected photodetectivity (*D**) are employed to evacuate the device performance of PDs. *R* is defined as: $R = \frac{J_{ph}}{L_{light}}$ and *D** is described as: $D^* = \frac{R}{\sqrt{2qJ_d}}$ (where $L_{light}$ is the light intensity and *q* is the absolute value of electron charge).[73] At $\lambda$ = 500 nm and under an external bias at –0.5 V, the *R* and *D** are summarized in Table 2. The *R* is increased up to 858 mA $W^{-1}$ for PPDs by the EMF-aligned $CH_3NH_3PbI_3$:$Fe_3O_4$ composite thin film from 389 for PPDs by the $CH_3NH_3PbI_3$:$Fe_3O_4$ composite thin film, and 145 mA $W^{-1}$ for PPDs by pristine $CH_3NH_3PbI_3$ thin film. The *D** is boosted to $2.4 \times 10^{13}$ Jones (1 Jones = 1 cm $Hz^{1/2}$ $W^{-1}$) for PPDs by the EMF-aligned $CH_3NH_3PbI_3$:$Fe_3O_4$ composite thin film from $9.79 \times 10^{12}$ PPDs by the $CH_3NH_3PbI_3$:$Fe_3O_4$ composite thin film and $3.16 \times 10^{12}$ Jones for PPDs by pristine $CH_3NH_3PbI_3$ thin film. Both enhanced *R* and *D** are a consequence of both improved $J_{ph}$ and reduced $J_d$.

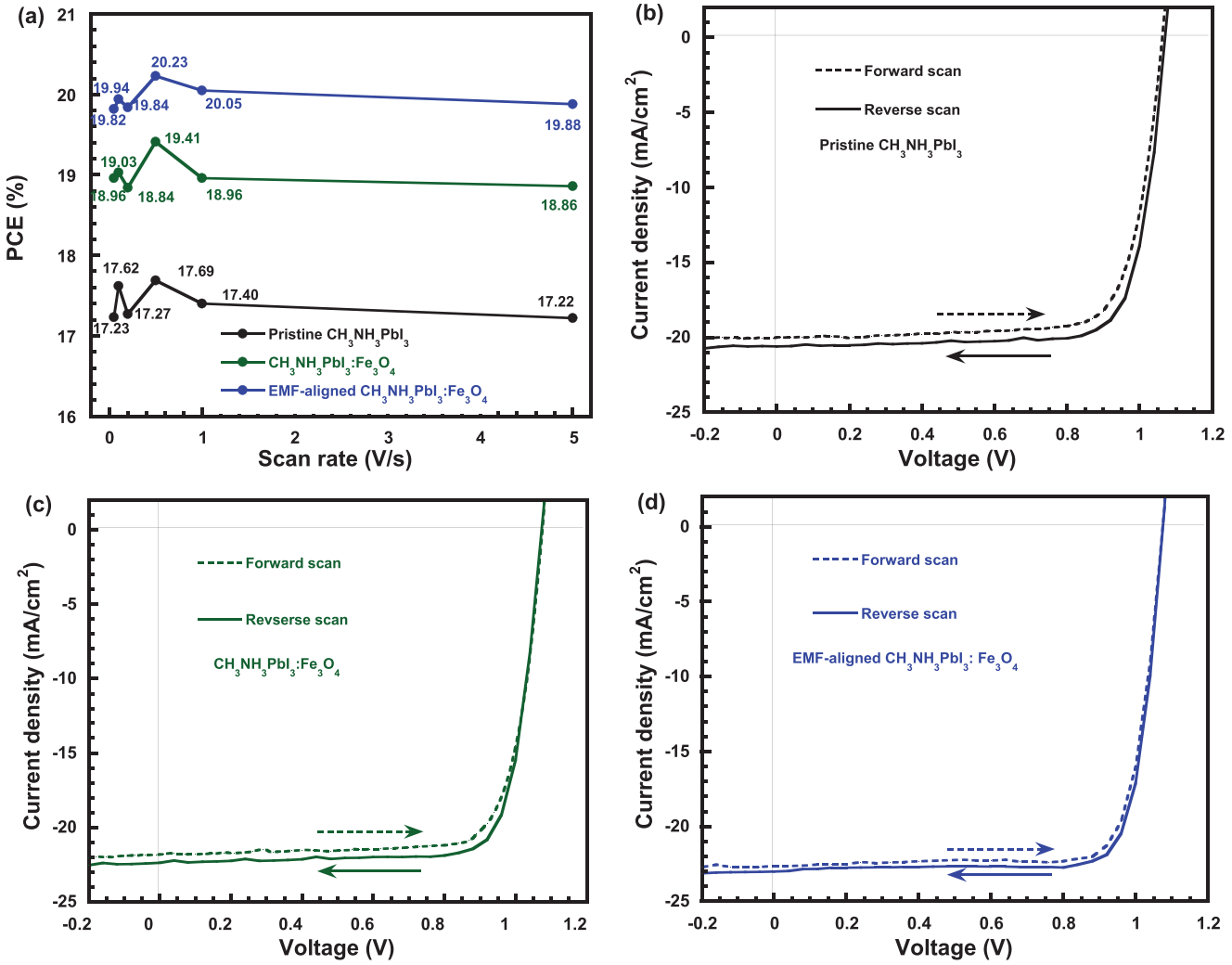


**Figure 5.** a) PCEs as the function of different scan rates under the reverse scan direction, hysteresis behaviors of b) PSCs by pristine $CH_3NH_3PbI_3$ thin film, c) PSCs by the $CH_3NH_3PbI_3$:$Fe_3O_4$ thin film, and d) PSCs by the EMF-aligned $CH_3NH_3PbI_3$:$Fe_3O_4$ thin film.

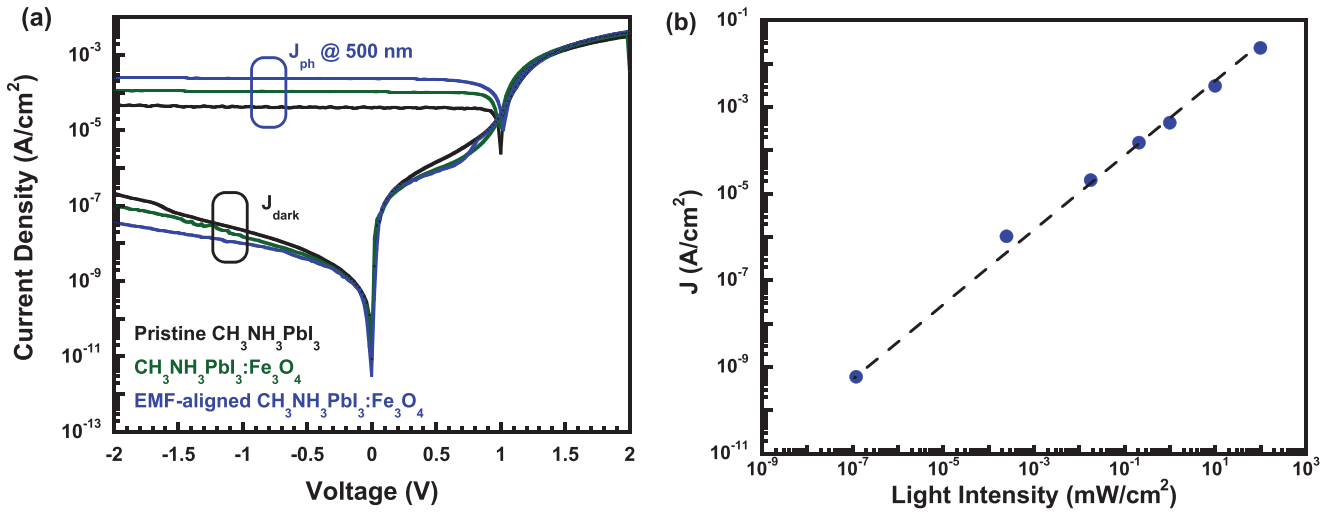


**Figure 6.** a) The *J–V* characteristics of PPDs measured both in dark and under the monochromatic light at the wavelength of 500 nm with the light intensity of 0.28 mW $cm^{-2}$ at room temperature, b) the LDR of PPDs by the EMF-aligned $CH_3NH_3PbI_3$:$Fe_3O_4$ thin film, where PPDs are fabricated by either pristine $CH_3NH_3PbI_3$ thin film, or the $CH_3NH_3PbI_3$:$Fe_3O_4$ thin film, or the EMF-aligned $CH_3NH_3PbI_3$:$Fe_3O_4$ thin film.

**Table 2.** Device performance parameters of PPDs.

| Photoactive layers | $J_{ph}$[a)] [A cm$^{-2}$] | $J_d$[a)] [A cm$^{-2}$] | $R$ [A W$^{-1}$] | $D^*$ [Jones] |
|---|---|---|---|---|
| Pristine $CH_3NH_3PbI_3$ | $4.06 \times 10^{-5}$ | $6.09 \times 10^{-9}$ | 0.145 | $3.22 \times 10^{12}$ |
| $CH_3NH_3PbI_3$:$Fe_3O_4$ | $1.09 \times 10^{-4}$ | $4.71 \times 10^{-9}$ | 0.389 | $9.79 \times 10^{12}$ |
| EMF-aligned $CH_3NH_3PbI_3$:$Fe_3O_4$ | $2.40 \times 10^{-4}$ | $3.84 \times 10^{-9}$ | 0.858 | $2.40 \times 10^{13}$ |

[a)] $J_{ph}$ is measured at $\lambda$ of 500 nm with the light intensity of 0.28 mW cm$^{-2}$ and under a bias of – 0.5 V; $J_d$ is measured in dark and under a bias of –0.5 V.

A linear dynamic range (LDR) or photosensitivity linearity (typically quoted in dB), one typical figure-of-merit that used to evaluate PDs performance, is also investigated. LDR is given by $\mathrm{LDR} = 20\log(J^*_{ph}/J_d)$,[73] where $J^*_{ph}$ is the photocurrent measured at the light intensity of 1 mW cm$^{-2}$. The photocurrent density versus the incident light intensity of PPDs by the EMF-aligned $CH_3NH_3PbI_3$:$Fe_3O_4$ composite thin film is presented in Figure 6b. At room temperature, an LDR of ≈162 dB is observed. Such high LDR is higher than that of Si PDs (120 dB) and is significantly higher than that of InGaAs PDs (66 dB) as well.[74]

## 3. Conclusions

In this study, we reported enhanced device performance of perovskite photovoltaics by the EMF-aligned $CH_3NH_3PbI_3$:$Fe_3O_4$ MNPs composite thin films. It was found that the EMF-aligned $CH_3NH_3PbI_3$:$Fe_3O_4$ composite thin films possess superior film morphology, boosted charge carrier mobility, and suppressed trap density. Moreover, perovskite photovoltaics by the EMF-aligned $CH_3NH_3PbI_3$:$Fe_3O_4$ composite thin film exhibited suppressed charge carrier recombination and shorter charge carrier extraction time. As a result, PSCs by the EMF-aligned $CH_3NH_3PbI_3$:$Fe_3O_4$ composite thin film exhibited 20.23% efficiency, which was ≈15% enhancement as compared with that by pristine $CH_3NH_3PbI_3$ thin film. Moreover, PSCs by the EMF-aligned $CH_3NH_3PbI_3$:$Fe_3O_4$ composite thin film exhibited significantly reduced photocurrent hysteresis. In addition, PPDs by the EMF-aligned $CH_3NH_3PbI_3$:$Fe_3O_4$ composite thin film exhibited a photoresponsivity of 858 mA W$^{-1}$, a photodetectivity over $10^{13}$ Jones, and linear dynamic range over 160 dB at room temperature. All these results demonstrated that we developed a facile way to boost device performance of perovskite photovoltaics.

## 4. Experimental Section

*Materials*: Lead iodide ($PbI_2$, 99.9985% metals basis) was purchased from Alfa Aesar. Phenyl-C61-butyric acid methyl ester ($PC_{61}BM$) (99.5%) was purchased from Solenne BV. $Fe(acac)_3$ (99%) was purchased from Acros. Triethylene glycol (TREG), poly[bis(4-phenyl)(2,4,6-trimethylphenyl)amine] (PTAA), bathocuproine (BCP), *N*,*N*-dimethylformamide (DMF, anhydrous, 99.8%), toluene (anhydrous, 99.8%), ethanol (anhydrous, > 99.5%), and chlorobenzene (anhydrous, 99.8%) were purchased from Sigma-Aldrich. All materials were used as received without further purification. Methylammonium iodide (MAI, $CH_3NH_3I$) was synthesized by hydroiodic acid and methylamine in laboratory.[6,7,39–41]

*Preparation of Perovskite Precursor Solutions*: $PbI_2$ was dissolved into DMF with a concentration of 400 mg mL$^{-1}$. $Fe_3O_4$ was dispersed in ethanol with 1 mg mL$^{-1}$. MAI without or with different volume ratio of $Fe_3O_4$-ethanol (the volume ratio of ethanol-$Fe_3O_4$ to ethanol were 3%, 6%, 9%, 12%, and 15%) was dissolved in ethanol with 35 mg mL$^{-1}$. Then, these precursor solutions were magnetically stirred at 75 °C overnight yielding to clear solutions.

*Thin Film Characterizations*: The TRPL spectra were obtained with a 532 nm pulsed laser as excitation source at a frequency of 9.743 MHz. The top view SEM images were obtained by using a field emission scanning electron microscope (JEOL-7401). UV-vis absorption spectra of different films were measured using the HP 8453 spectrophotometer. The GIWAXS investigation was performed on the dedicated high-resolution GIWAXS beamline (Sector 8-ID-E) in the Advanced Photon Source (APS) Argonne National Laboratory. The thickness of thin films was measured by Dektak 150 surface profilometer with the scan rate of 0.06 mm s$^{-1}$.

*Photovoltaic Devices Fabrication*: After precleaned ITO substrates were treated with UV ozone for 40 min under an ambient atmosphere, then transferred into glovebox with nitrogen atmosphere, ≈10 nm PTAA was spin coated on the top of ITO substrates with a spin speed of 6000 rpm for 40 s from PTAA toluene solution (2 mg mL$^{-1}$), followed with thermal annealing at 100 °C for 10 min. The perovskite active layer was prepared by a two-step method.[5,6,34–36] First, $PbI_2$ layer was spin-casted on the top of preheated (80 °C) PTAA/ITO substrates from the warm (80 °C) $PbI_2$ solution at a spin speed of 6000 rpm for 20 s with an acceleration time of 2 s. Then the substrates were heated on the hotplate at 80 °C for 10 min and cooled down to room temperature. The MAI (or MAI:x$Fe_3O_4$) layer was then spin-coated on the top of $PbI_2$ layers from the MAI (or MAI:x$Fe_3O_4$) precursor solution at a spin speed of 6000 rpm for 35 s with an acceleration time of 5 s, followed with a thermal annealing at 100 °C for 2 h. After perovskite thin film was cooled down to room temperature naturally, an ≈60 nm $PC_{61}BM$ was spin-coated on the top of perovskite layer at a spin speed of 1500 rpm for 30 s with an acceleration time of 2 s from the $PC_{61}BM$ chlorobenzene solution (20 mg mL$^{-1}$). Afterward, an ≈8 nm BCP thin layer was spin-coated on the top of $PC_{61}B6M$ with a spin speed of 4000 rpm for 30 s from 0.5 mg mL$^{-1}$ ethanol solution. Lastly, an ≈100 nm thick Al (aluminum) was thermally deposited through a shadow mask in the vacuum with the press of $2 \times 10^{-6}$ mbar. The device area was measured to be 0.045 cm$^2$.

*Photovoltaic Devices Characterizations*: The current density–voltage (*J*–*V*) characteristics were obtained by using a Keithley model 2400 source measure unit. A Newport Air Mass 1.5 Global (AM1.5G) full-spectrum solar simulator was applied as the light source. The light intensity was 100 mW cm$^{-2}$, which was calibrated by utilizing a monosilicon detector (with a KG-5 visible color filter) of National Renewable Energy Laboratory to reduce the spectral mismatch. The EQE spectra of the PSCs were measured through the EQE measurement setup (DSR100UV-B) in use at ESTI for cells and mini-modules. A 300 W steady-state xenon lamp provided the source light. The impedance spectra (IS) of solar cells were obtained using an HP 4194A impedance/gain-phase analyzer in dark, with an oscillating voltage of 10 mV from 5 to $10^5$ Hz. Solar cells were held at the voltage closing to the corresponding $V_{OC}$, while the IS was carried out. The TPC measurements were conducted on home-made setup reported in previous reports.[39–41]

## Supporting Information

Supporting Information is available from the Wiley Online Library or from the author.

## Acknowledgements

W.X. and T.Z. contributed equally to this work. The authors at the University of Akron thank National Science Foundation (EECs 1903303) and Air Force Office of Scientific Research (AFOSR) (through the Organic Materials Chemistry Program, Grant Number: FA9550-15-1-0292, Program Manager, Dr. Kenneth Caster) for financial supports.

## Conflict of Interest

The authors declare no conflict of interest.

## Keywords

device performance, external magnetic field, magnetic nanoparticles, perovskite photodetectors, perovskite solar cells

Received: March 29, 2020
Revised: April 17, 2020
Published online:

[1] Q. Jiang, Y. Zhao, X. Zhang, X. Yang, Y. Chen, Z. Chu, Q. Ye, X. Li, Z. Yin, J. You, *Nat. Photonics* **2019**, *13*, 460.
[2] S. Mahesh, J. M. Ball, R. D. Oliver, D. P. McMeekin, P. K. Nayak, M. B. Johnston, H. J. Snaith, *Energy Environ. Sci.* **2020**, *13*, 258.
[3] P. You, G. Li, G. Tang, J. Cao, F. Yan, *Energy Environ. Sci.* **2020**, *13*, 1187.
[4] N. Wang, W. Liu, Q. Zhang, *Small Methods* **2018**, *2*, 1700380.
[5] Z. Xu, Y. Yu, S. Arya, I. A. Niaz, Y. Chen, Y. Lei, M. A. R. Miah, J. Zhou, A. C. Zhang, L. Yan, *Nano Lett.* **2020**, *20*, 2144.
[6] W. Xu, Y. Guo, X. Zhang, L. Zheng, T. Zhu, D. Zhao, W. Hu, X. Gong, *Adv. Funct. Mater.* **2018**, *28*, 1705541.
[7] T. Zhu, Y. Yang, L. Zheng, L. Liu, M. L. Becker, X. Gong, *Adv. Funct. Mater.* **2020**, *30*, 1909487.
[8] M. He, B. Li, X. Cui, B. Jiang, Y. He, Y. Chen, D. O'Neil, P. Szymanski, M. A. Ei-Sayed, J. Huang, Z. Lin, *Nat. Commun.* **2017**, *8*, 16045.
[9] P.-Y. Gu, N. Wang, C. Wang, Y. Zhou, G. Long, M. Tian, W. Chen, X. W. Sun, M. G. Kanatzidis, Q. Zhang, *J. Mater. Chem. A* **2017**, *5*, 7339.
[10] A. A. Said, J. Xie, Q. Zhang, *Small* **2019**, *15*, 1900854.
[11] A. Miyata, A. Mitioglu, P. Plochocka, O. Portugall, J. T.-W. Wang, S. D. Stranks, H. J. Snaith, R. Nicholas, *Nat. Phys.* **2015**, *11*, 582.
[12] P. Y. Gu, N. Wang, A. Wu, Z. Wang, M. Tian, Z. Fu, X. W. Sun, Q. Zhang, *Chem. - Asian J.* **2016**, *11*, 2135.
[13] M. Zhang, X. Cui, Y. Wang, B. Wang, M. Ye, W. Wang, C. Ma, Z. Lin, *Nano Energy* **2020**, *71*, 104620.
[14] B. Wang, M. Zhang, X. Cui, Z. Wang, M. Rager, Y. Yang, Z. Zou, Z. Wang, Z. Lin, *Angew. Chem., Int. Ed.* **2020**, *59*, 1611.
[15] X. Cui, Y. Chen, M. Zhang, Y. W. Harn, J. Qi, L. Gao, Z. Wang, Y. Yang, Z. Lin, *Energy Environ. Sci.* **2020**. https://doi.org/10.1039/c9ee03937f.
[16] N. Wang, K. Zhao, T. Ding, W. Liu, A. S. Ahmed, Z. Wang, M. Tian, X. Sun, Q. Zhang, *Adv. Energy Mater.* **2017**, *7*, 1700522.
[17] A. Kojima, K. Teshima, Y. Shirai, T. Miyasaka, *J. Am. Chem. Soc.* **2009**, *131*, 6050.
[18] W. S. Yang, J. H. Noh, N. J. Jeon, Y. C. Kim, S. Ryu, J. Seo, S. I. Seok, *Science* **2015**, *348*, 1234.
[19] K. Sun, Z. Hu, B. Shen, C. Lu, C. Yang, C. Gao, J. Zhang, Y. Zhu, *Sol. Energy Mater. Sol. Cells* **2018**, *185*, 464.
[20] D.-Y. Son, J.-W. Lee, Y. J. Choi, I.-H. Jang, S. Lee, P. J. Yoo, H. Shin, N. Ahn, M. Choi, D. Kim, *Nat. Energy* **2016**, *1*, 16081.
[21] H. Tan, A. Jain, O. Voznyy, X. Lan, F. P. G. De Arquer, J. Z. Fan, R. Quintero-Bermudez, M. Yuan, B. Zhang, Y. Zhao, *Science* **2017**, *355*, 722.
[22] W. S. Yang, B.-W. Park, E. H. Jung, N. J. Jeon, Y. C. Kim, D. U. Lee, S. S. Shin, J. Seo, E. K. Kim, J. H. Noh, *Science* **2017**, *356*, 1376.
[23] K. Wojciechowski, S. D. Stranks, A. Abate, G. Sadoughi, A. Sadhanala, N. Kopidakis, G. Rumbles, C.-Z. Li, R. H. Friend, H. J. Snaith, *ACS Nano* **2014**, *8*, 12701.
[24] Best Research-Cell Efficiencies, https://www.nrel.gov/pv/assets/pdfs/best-research-cell-efficiencies.20200406.pdf (accessed: April 2020).
[25] D. Bi, W. Tress, M. I. Dar, P. Gao, J. Luo, C. Renevier, K. Schenk, A. Abate, F. Giordano, J.-P. C. Baena, *Sci. Adv.* **2016**, *2*, e1501170.
[26] A. Buin, R. Comin, J. Xu, A. H. Ip, E. H. Sargent, *Chem. Mater.* **2015**, *27*, 4405.
[27] A. Abate, M. Saliba, D. J. Hollman, S. D. Stranks, K. Wojciechowski, R. Avolio, G. Grancini, A. Petrozza, H. Snaith, *Nano Lett.* **2014**, *14*, 3247.
[28] I. Sokolik, E. Frankevich, *Sov. Phys. Usp.* **1974**, *16*, 687.
[29] C.-J. Sun, Y. Wu, Z. Xu, B. Hu, J. Bai, J.-P. Wang, J. Shen, *Appl. Phys. Lett.* **2007**, *90*, 232110.
[30] W. Zhang, Y. Xu, H. Wang, C. Xu, S. Yang, S. Cells, *Sol. Energy Mater. Sol. Cells* **2011**, *95*, 2880.
[31] K. Wang, C. Yi, C. Liu, X. Hu, S. Chuang, X. Gong, *Sci. Rep.* **2015**, *5*, 9265.
[32] D. M. González, V. Körstgens, Y. Yao, L. Song, G. Santoro, S. V. Roth, P. Müller-Buschbaum, *Adv. Energy Mater.* **2015**, *5*, 1401770.
[33] Y. C. Hsiao, T. Wu, M. Li, B. Hu, *Adv. Mater.* **2015**, *27*, 2899.
[34] C. Zhang, D. Sun, C. Sheng, Y. Zhai, K. Mielczarek, A. Zakhidov, Z. Vardeny, *Nat. Phys.* **2015**, *11*, 427.
[35] H. Wang, J. Lei, F. Gao, Z. Yang, D. Yang, J. Jiang, J. Li, X. Hu, X. Ren, B. Liu, J. Liu, H. Lei, Z. Liu, S. Liu, *ACS Appl. Mater. Interfaces* **2017**, *9*, 21756.
[36] Y. Kim, E. H. Jung, G. Kim, D. Kim, B. J. Kim, J. Seo, *Adv. Energy Mater.* **2018**, *8*, 1801668.
[37] W. Cai, J. Wan, *J. Colloid Interface Sci.* **2007**, *305*, 366.
[38] C. Bi, Q. Wang, Y. Shao, Y. Yuan, Z. Xiao, J. Huang, *Nat. Commun.* **2015**, *6*, 7747.
[39] K. Wang, L. Zheng, T. Zhu, L. Liu, M. L. Becker, X. Gong, *Nano Energy* **2020**, *67*, 104229.
[40] W. Xu, L. Zheng, T. Zhu, L. Liu, X. Gong, *ACS Appl. Mater. Interfaces* **2019**, *11*, 34020.
[41] W. Xu, L. Zheng, X. Zhang, Y. Cao, T. Meng, D. Wu, L. Liu, W. Hu, X. Gong, *Adv. Energy Mater.* **2018**, *8*, 1703178.
[42] X. Yao, L. Zheng, X. Zhang, W. Xu, W. Hu, X. Gong, *ACS Appl. Mater. Interfaces* **2019**, *11*, 40163.
[43] J. C. Yu, D. B. Kim, G. Baek, B. R. Lee, E. D. Jung, S. Lee, J. H. Chu, D. K. Lee, K. J. Choi, S. Cho, M. H. Song, *Adv. Mater.* **2015**, *27*, 3492.
[44] W. Nie, H. Tsai, R. Asadpour, J. C. Blancon, A. J. Neukirch, G. Gupta, J. J. Crochet, M. Chhowalla, S. Tretiak, M. A. Alam, H. L. Wang, A. D. Mohite, *Science* **2015**, *347*, 522.
[45] J. Cao, B. Wu, R. Chen, Y. Wu, Y. Hui, B. W. Mao, N. Zheng, *Adv. Mater.* **2018**, *30*, 1705596.
[46] Z. Zhou, Z. Wang, Y. Zhou, S. Pang, D. Wang, H. Xu, Z. Liu, N. P. Padture, G. Cui, *Angew. Chem., Int. Ed.* **2015**, *54*, 9705.
[47] J. Qi, X. Yao, W. Xu, X. Wu, X. Jiang, X. Gong, Y. Cao, *ACS Omega* **2018**, *3*, 7069.
[48] Y. Kutes, L. Ye, Y. Zhou, S. Pang, B. D. Huey, N. P. Padture, *J. Phys. Chem. Lett.* **2014**, *5*, 3335.
[49] W. Zhang, M. Saliba, D. T. Moore, S. K. Pathak, M. T. Horantner, T. Stergiopoulos, S. D. Stranks, G. E. Eperon, J. A. Alexander-Webber, A. Abate, A. Sadhanala, S. Yao, Y. Chen, R. H. Friend, L. A. Estroff, U. Wiesner, H. J. Snaith, *Nat. Commun.* **2015**, *6*, 6142.
[50] A. Sharenko, M. F. Toney, *J. Am. Chem. Soc.* **2016**, *138*, 463.

 

[51] B. P. Dhamaniya, P. Chhillar, B. Roose, V. Dutta, S. K. Pathak, *ACS Appl. Mater. Interfaces* **2019**, *11*, 22228.
[52] J. S. Park, S. Choi, Y. Yan, Y. Yang, J. M. Luther, S. H. Wei, P. Parilla, K. Zhu, *J. Phys. Chem. Lett.* **2015**, *6*, 4304.
[53] P. N. Murgatroyd, *J. Phys. D: Appl. Phys.* **1970**, *3*, 151.
[54] R. H. Bube, *J. Appl. Phys.* **1962**, *33*, 1733.
[55] P. P. Boix, G. Garcia-Belmonte, U. Munecas, M. Neophytou, C. Waldauf, R. Pacios, *Appl. Phys. Lett.* **2009**, *95*, 233302.
[56] G. Xing, N. Mathews, S. Sun, S. S. Lim, Y. M. Lam, M. Gratzel, S. Mhaisalkar, T. C. Sum, *Science* **2013**, *342*, 344.
[57] J. Feng, X. Yan, Y. Liu, H. Gao, Y. Wu, B. Su, L. Jiang, *Adv. Mater.* **2017**, *29*, 1605993.
[58] J. S. Manser, P. V. Kamat, *Nat. Photonics* **2014**, *8*, 737.
[59] E. A. Duijnstee, J. M. Ball, V. M. Le Corre, L. J. A. Koster, H. J. Snaith, J. Lim, *ACS Energy Lett.* **2020**, *5*, 376.
[60] N. Ahn, D. Y. Son, I. H. Jang, S. M. Kang, M. Choi, N. G. Park, *J. Am. Chem. Soc.* **2015**, *137*, 8696.
[61] V. Gonzalez-Pedro, E. J. Juarez-Perez, W. S. Arsyad, E. M. Barea, F. Fabregat-Santiago, I. Mora-Sero, J. Bisquert, *Nano Lett.* **2014**, *14*, 888.
[62] L. Zheng, S. Mukherjee, K. Wang, M. E. Hay, B. W. Boudouris, X. Gong, *J. Mater. Chem. A* **2017**, *5*, 23831.
[63] J. Qiu, S. Yang, *Chem. Rec.* **2020**, *20*, 209.
[64] H. Taherianfard, G. W. Kim, F. Ebadi, T. Abzieher, K. Choi, U. W. Paetzold, B. S. Richards, A. Alrhman Eliwi, F. Tajabadi, N. Taghavinia, M. Malekshahi Byranvand, *ACS Appl. Mater. Interfaces* **2019**, *11*, 44802.
[65] N. Li, B. E. Lassiter, R. R. Lunt, G. Wei, S. R. Forrest, *Appl. Phys. Lett.* **2009**, *94*, 13.
[66] S. R. Cowan, A. Roy, A. J. Heeger, *Phys. Rev. B* **2010**, *82*, 245207.
[67] S. R. Cowan, N. Banerji, W. L. Leong, A. J. Heeger, *Adv. Funct. Mater.* **2012**, *22*, 1116.
[68] J. Seifter, Y. Sun, H. Choi, B. H. Lee, T. L. Nguyen, H. Y. Woo, A. J. Heeger, *Adv. Mater.* **2015**, *27*, 4989.
[69] J. Seifter, Y. Sun, A. J. Heeger, *Adv. Mater.* **2014**, *26*, 2486.
[70] J. Xiong, B. Yang, R. Wu, C. Cao, Y. Huang, C. Liu, Z. Hu, H. Huang, Y. Gao, J. Yang, *Org. Electron.* **2015**, *24*, 106.
[71] J. Wei, Y. Zhao, H. Li, G. Li, J. Pan, D. Xu, Q. Zhao, D. Yu, *J. Phys. Chem. Lett.* **2014**, *5*, 3937.
[72] H. S. Kim, N. G. Park, *J. Phys. Chem. Lett.* **2014**, *5*, 2927.
[73] X. Gong, M. Tong, Y. Xia, W. Cai, J. S. Moon, Y. Cao, G. Yu, C. L. Shieh, B. Nilsson, A. J. Heeger, *Science* **2009**, *325*, 1665.
[74] A. R. Jha, *Infrared Technology: Applications in Electro-Optics, Photonics Devices, and Sensors*, Wiley, New York **2000**.